

DIFFUSION ADVERSARIAL REPRESENTATION LEARNING FOR SELF-SUPERVISED VESSEL SEGMENTATION

Boah Kim*, Yujin Oh*, Jong Chul Ye

Korea Advanced Institute of Science and Technology (KAIST), Daejeon, Republic of Korea
 {boahkim, yujin.oh, jong.ye}@kaist.ac.kr

ABSTRACT

Vessel segmentation in medical images is one of the important tasks in the diagnosis of vascular diseases and therapy planning. Although learning-based segmentation approaches have been extensively studied, a large amount of ground-truth labels are required in supervised methods and confusing background structures make neural networks hard to segment vessels in an unsupervised manner. To address this, here we introduce a novel diffusion adversarial representation learning (DARL) model that leverages a denoising diffusion probabilistic model with adversarial learning, and apply it for vessel segmentation. In particular, for self-supervised vessel segmentation, DARL learns background image distribution using a diffusion module, which lets a generation module effectively provide vessel representations. Also, by adversarial learning based on the proposed switchable spatially-adaptive denormalization, our model estimates synthetic fake vessel images as well as vessel segmentation masks, which further makes the model capture vessel-relevant semantic information. Once the proposed model is trained, the model generates segmentation masks by one step and can be applied to general vascular structure segmentation of coronary angiography and retinal images. Experimental results on various datasets show that our method significantly outperforms existing unsupervised and self-supervised methods in vessel segmentation.

1 INTRODUCTION

In the clinical diagnosis of vascular diseases, vessel segmentation is necessary to analyze the vessel structures and therapy planning. In particular, when diagnosing coronary artery disease, X-ray angiography is taken to enhance vessel visualization by injecting a contrast agent into the blood vessels (Cong et al., 2015). However, it is challenging to extract vessels accurately due to low contrast, motion artifacts, many tiny branches, structural interference in the backgrounds, etc (Xia et al., 2019; Chen et al., 2014).

To segment vascular structures, various segmentation methods have been explored. Traditional optimization models (Law & Chung, 2009; Taghizadeh Dehkordi et al., 2014) typically require complicated preprocessing steps and manual tuning. Furthermore, they are computationally expensive to process many images. On the other hand, learning-based methods (Nasr-Esfahani et al., 2016; Fan et al., 2018; Chen et al., 2019) generate segmentation maps in real-time once the models are trained. However, supervised methods require a huge amount of labeled data for training, which complicates their use in practical applications. Also, existing unsupervised methods designed on natural images are difficult to apply to medical vessel images due to low contrast subtle branches and confusing background structures. Although a recent self-supervised method (Ma et al., 2021) is presented to learn vessel representations, this requires two different adversarial networks to segment vessels, which leads to increasing training complexity.

Recently, diffusion models such as denoising diffusion probabilistic model (DDPM) (Ho et al., 2020) has become one of the main research topics in modeling data distribution and sampling diverse images. By learning the Markov transformation of the reverse diffusion process from Gaussian noise to data, DDPM is successfully applied to many low-level computer vision tasks such as super-resolution (Chung et al., 2022), inpainting (Lugmayr et al., 2022), and colorization (Song et al.,

* Co-first authors

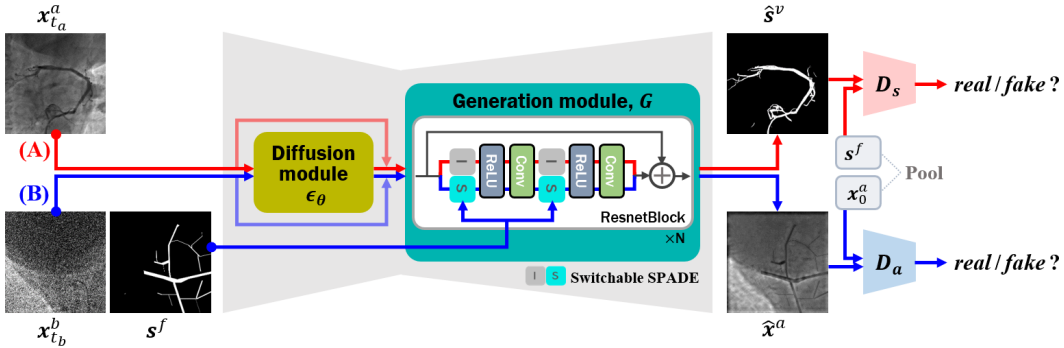


Figure 1: Our proposed diffusion adversarial representation model for self-supervised vessel segmentation. In path (A), given a real noisy angiography image $x_{t_a}^a$, our model estimates vessel segmentation masks \hat{s}^v . In path (B), given a real noisy background image $x_{t_b}^b$ and a vessel-like fractal mask s^f , our model generates a synthetic angiography image \hat{x}^a .

2020). For high-level vision tasks, while a recent study (Baranchuk et al., 2021) shows that DDPM can capture semantic information and be used as image representations, methods applying DDPM in learning semantic segmentation without labeled data have so far not been developed.

In this paper, we introduce a novel concept of diffusion adversarial representation learning (DARL), which is a non-iterative version of diffusion-based generative model that can be successfully applied to self-supervised vessel segmentation. As illustrated in Figure 1, our model is composed of a diffusion module and a generation module, which learns semantic information of vessels via adversarial learning without ground-truth labels. In particular, given unpaired data of background images and angiography images that are taken before and after injection of the contrast agent, the diffusion module is designed to learn the background image distribution. Also, inspired by the spatially-adaptive denormalization (SPADE) layer (Park et al., 2019) that is effective in image synthesis given semantic masks, we design a *switchable* version of SPADE as the generation module to estimate vessel segmentation masks as well as fake angiograms using the synthetic fractal masks (Ma et al., 2021).

More specifically, as shown in Figure 1, there are two paths for feeding the inputs into our proposed model: (A) when the real angiography images are given, our model without the SPADE estimates vessel segmentation masks; (B) when the background images are given, our model with the SPADE generates synthetic angiograms that composite fake vessel masks such as fractal masks with the input backgrounds. Also, by feeding the generated angiograms into the (A) path, we apply the cycle consistency between the segmentation results of the synthetic angiograms and the inputted fake vessel masks to capture semantic information of vessels. Since the diffusion module learns the background distribution, the foreground vessel structures of angiograms are considered as outlier noise so that latent features from the diffusion module can isolate the vessel representations. This enables the generation module to effectively segment the vessels.

We build our model on X-ray coronary angiography using XCAD dataset (Ma et al., 2021) and apply to several different blood vessel datasets, including retinal images. Experimental results show that our method outperforms existing unsupervised and self-supervised learning methods in the absence of labeled data for training. The main contributions are summarized as:

1. We propose a diffusion adversarial representation model, a non-iterative version of diffusion model for image generation, and apply it for self-supervised vessel segmentation. Specifically, the latent features of our diffusion module provide vessel information and thus improve the segmentation performance.
2. Through the proposed generation module with switchable SPADE layers, our model not only generates synthetic angiography images but also segments vessel structures.
3. Experimental results verify that our model achieves superior segmentation performance by learning vessel representations. In particular, although the model is trained using X-ray coronary angiograms, it provides the state-of-the-art performance for un-/self-supervised retinal vessel segmentation as well, confirming the generalization capability of the model.

2 BACKGROUNDS AND RELATED WORKS

Denoising diffusion probabilistic model Diffusion model (Sohl-Dickstein et al., 2015; Ho et al., 2020; Song & Ermon, 2019) is one of generative models that sample realistic data by learning the distribution of real images. In particular, the denoising diffusion probabilistic model (DDPM) (Ho et al., 2020) with a score matching has been shown superior performance in image generation. Specifically, DDPM learns the Markov chain to convert the Gaussian noise distribution $\mathbf{x}_T \sim \mathcal{N}(\mathbf{0}, \mathbf{I})$ into the target distribution \mathbf{x}_0 . In the forward diffusion process, the noise is gradually added the noise to the data by:

$$q(\mathbf{x}_t | \mathbf{x}_{t-1}) = \mathcal{N}(\mathbf{x}_t; \sqrt{1 - \beta_t} \mathbf{x}_{t-1}, \beta_t \mathbf{I}), \quad (1)$$

where $\beta_t \in [0, 1]$ is a fixed variance. Accordingly, a noisy target \mathbf{x}_t distribution from the data \mathbf{x}_0 is represented as:

$$q(\mathbf{x}_t | \mathbf{x}_0) = \mathcal{N}(\mathbf{x}_t; \sqrt{\alpha_t} \mathbf{x}_0, (1 - \alpha_t) \mathbf{I}), \quad (2)$$

where $\alpha_t = \prod_{s=1}^t (1 - \beta_s)$. Then, DDPM is trained to approximate reverse diffusion process:

$$p_\theta(\mathbf{x}_{t-1} | \mathbf{x}_t) = \mathcal{N}(\mathbf{x}_{t-1}; \boldsymbol{\mu}_\theta(\mathbf{x}_t, t), \sigma_t^2 \mathbf{I}), \quad (3)$$

where σ_t is a fixed variance, and $\boldsymbol{\mu}_\theta$ is a parameterized mean with the noise predictor $\boldsymbol{\epsilon}_\theta$:

$$\boldsymbol{\mu}_\theta(\mathbf{x}_t, t) = \frac{1}{\sqrt{1 - \beta_t}} \left(\mathbf{x}_t - \frac{\beta_t}{\sqrt{1 - \alpha_t}} \boldsymbol{\epsilon}_\theta(\mathbf{x}_t, t) \right). \quad (4)$$

Thus, in the generative process, the sample can be obtained from the Gaussian noise by the iterative denoising steps: $\mathbf{x}_{t-1} = \boldsymbol{\mu}_\theta(\mathbf{x}_t, t) + \sigma_t \mathbf{z}$, where $\mathbf{z} \sim \mathcal{N}(0, \mathbf{I})$.

Through this stochastic process, DDPM provides diverse realistic samples and has been exploited in many applications, including super-resolution (Chung et al., 2022; Saharia et al., 2021), inpainting (Lugmayr et al., 2022), and colorization (Song et al., 2020; Saharia et al., 2022). However, the application study of semantic segmentation is limited. Although several works (Baranchuk et al., 2021; Amit et al., 2021) are recently presented to solve high-level vision problems, they require annotated data to train the models.

Self-supervised vessel segmentation For the vessel segmentation task, it is difficult to obtain fine-grained labels for supervised learning, since the vessel has complex structures with numerous tiny branches. While this label scarcity issue can be alleviated by semi- or unsupervised learning, fully unsupervised methods to segment the tiny vessels with reasonable performance are relatively scarce. In fact, recent unsupervised learning methods trained with natural images have great generalization capability on unseen datasets (Ahn et al., 2021; Chen et al., 2019; Melas-Kyriazi et al., 2022), thus they can be easily adapted to medical image segmentation tasks. However, due to the unique characteristics of angiography, e.g. confusing background factors and sophisticated vessel structures, most unsupervised methods fail to endure drastic performance degradation when they are applied to vessel segmentation tasks. As a type of unsupervised learning, self-supervised learning also has been introduced to utilize self-generated supervisory labels from data themselves to efficiently learn target representations in various medical image segmentation tasks and has demonstrated its potential (Mahmood et al., 2019; Ma et al., 2021; Oh & Ye, 2021). Specifically, Ma et al. (2021) introduces an end-to-end adversarial learning framework for vessel segmentation with the CycleGAN (Zhu et al., 2017) structure, which learns realistic angiogram generation that adds fractal-guided pseudo labels to the background images. However, the simple arithmetic operation for synthetic vessel generation often fails to yield realistic pseudo-vessel images, thus training the adversarial networks using unrealistic synthetic images is difficult to produce optimal segmentation performance.

3 DIFFUSION ADVERSARIAL REPRESENTATION LEARNING

In this section, we describe our novel diffusion adversarial representation learning (DARL) model, tailored for self-supervised vessel segmentation method. As shown in Figure 1, DARL model is trained on unpaired real angiography images \mathbf{x}_0^a and real background images \mathbf{x}_0^b .

Specifically, our model is comprised of a diffusion module $\boldsymbol{\epsilon}_\theta$ to estimate latent features, a generation module G to estimate both the vessel segmentation masks $\hat{\mathbf{s}}^v$ and the synthetic angiograms $\hat{\mathbf{x}}^a$,

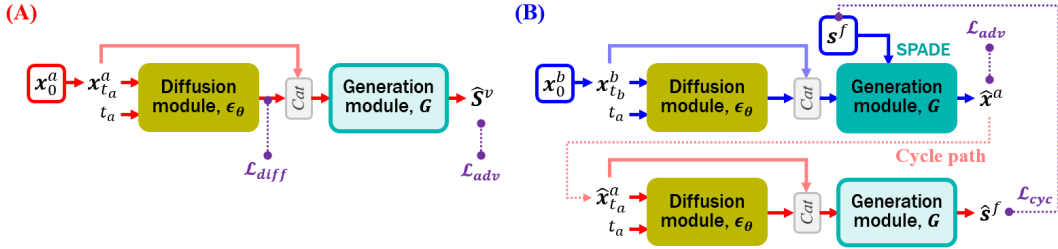


Figure 2: Training flow of our model. The generation module with the switchable SPADE layers takes ϵ_θ with the noisy images and generates desired outputs corresponding to the paths, i.e. (A) path for the angiography data to generate segmentation masks, and (B) path for the background images to generate the fake angiography images. The cycle path enables capturing the vessel information.

and two discriminators (D_s, D_a) to distinguish real and fake images of the vessel masks and the angiograms, respectively. Here, to generate fake angiograms, we design the generation module to synthesize the fake angiograms by combining fake vessel masks s^f with the background images, where the fake vessels are random fractal masks presented in Ma et al. (2021). In particular, we utilize the SPADE normalization layer (Park et al., 2019) that facilitates realistic image generation while preserving the semantic information of a given input mask. In the following, we explain the proposed generation module in detail, and then describe the model training and inference.

Generation module with switchable SPADE layer As illustrated in Figure 1, the proposed generation module consists of N residual blocks (ResnetBlock) that have switchable SPADE (S-SPADE) layers. Let $v \in \mathbb{R}^{M \times C \times H \times W}$ be the feature map in the ResnetBlock, where M, C, H , and W are the size of batch, channel, height, and width, respectively. Then, the switchable SPADE layer normalizes feature maps differently depending on the existence of an input mask s :

$$v = \begin{cases} \text{SPADE}(v, s), & \text{if mask } s \text{ is given,} \\ \text{IN}(v), & \text{otherwise,} \end{cases} \quad (5)$$

where IN is the instance normalization (Ulyanov et al., 2017). So, when our model is given the fake vessel mask s^f , the SPADE is computed by:

$$x_{m,c,h,w} = \gamma_{c,h,w}(s^f) \frac{x_{m,c,h,w} - \mu_c}{\sigma_c} + \beta_{c,h,w}(s^f), \quad (6)$$

where $x_{m,c,h,w}$ denotes the (m, c, h, w) -th element of the feature tensor v , (μ_c, σ_c) are the mean and standard deviation of the feature map in channel c , and $(\gamma_{c,h,w}, \beta_{c,h,w})$ are learned modulation parameters during training.

Thus, in the (A) path, given the noisy angiogram x_t^a and the latent feature $\epsilon_\theta(x_t^a, t)$, the generation module G estimates the vessel segmentation masks \hat{s}^v without the SPADE:

$$\hat{s}^v = G(\epsilon_\theta(x_t^a, t); \mathbf{0}). \quad (7)$$

On the other hand, in the (B) path that provides the fractal mask s^f , the generation module taking the noisy background x_t^b and its latent feature $G(\epsilon_\theta(x_t^b, t))$ synthesizes the fake angiograms \hat{x}^a :

$$\hat{x}^a = G(\epsilon_\theta(x_t^b, t); s^f). \quad (8)$$

3.1 NETWORK TRAINING

In contrast to the DDPM that pretrains the diffusion model, our method trains the diffusion module, generation module, and discriminators simultaneously using an adversarial learning framework. Figure 2 depicts the detailed training flow of our model. There are two distinct paths: (A) one feeds the real angiograms x_0^a into the model to provide vessel masks \hat{s}^v , and (B) the other takes the real backgrounds x_0^b and the fractal masks s^f for the model to generate fake angiograms \hat{x}^a . Here, as shown in Figure 2(B), since the input fractal masks can be regarded as vessel segmentation labels of the fake angiograms, we forward the fake angiograms generated through the (B) path to the (A) path, and apply cycle consistency between the estimated segmentation masks and the fractal masks to capture the vessel information.

3.1.1 LOSS FUNCTION

To train the model, we employ LSGAN (Mao et al., 2017) framework, which leads to the alternating application of the following two optimization problems:

$$\min_{\theta, G} \mathcal{L}^G(\epsilon_\theta, G, D_s, D_a), \quad \min_{D_s, D_a} \mathcal{L}^D(\epsilon_\theta, G, D_s, D_a), \quad (9)$$

where \mathcal{L}^G , and \mathcal{L}^D denotes the losses for the diffusion/generator and discriminator, respectively, which are given by:

$$\mathcal{L}^G(\epsilon_\theta, G, D_s, D_a) = \mathcal{L}_{diff}(\epsilon_\theta) + \alpha \mathcal{L}_{adv}^G(\epsilon_\theta, G, D_s, D_a) + \beta \mathcal{L}_{cyc}(\epsilon_\theta, G), \quad (10)$$

$$\mathcal{L}^D(\epsilon_\theta, G, D_s, D_a) = \mathcal{L}_{adv}^{D_s}(\epsilon_\theta, G, D_s) + \mathcal{L}_{adv}^{D_a}(\epsilon_\theta, G, D_a), \quad (11)$$

where α and β are hyperparameters, \mathcal{L}_{diff} is the diffusion loss, \mathcal{L}_{adv} is adversarial loss, and \mathcal{L}_{cyc} is cyclic reconstruction loss. The detailed description of each loss function is as follows.

Diffusion loss Recall that the diffusion module learns the distribution of images to estimate meaningful latent features of the inputs. We follow the standard loss for DDPM training (Ho et al., 2020):

$$\mathcal{L}_{diff}(\epsilon_\theta) := \mathbb{E}_{t, \mathbf{x}_0, \epsilon} \left[\|\epsilon - \epsilon_\theta(\sqrt{\alpha_t} \mathbf{x}_0 + \sqrt{1 - \alpha_t} \epsilon, t)\|^2 \right]. \quad (12)$$

where $\epsilon \sim \mathcal{N}(\mathbf{0}, \mathbf{I})$. In particular, to let the diffusion module represent the vessels of angiograms effectively, we define the diffusion loss on the background images, i.e. $\mathbf{x}_0 = \mathbf{x}_0^b$ in the (B) path and set the sampling schedule in $t \in [0, T]$. Accordingly, the diffusion module is trained intensively to learn the background image distribution, allowing the module in the (A) path to regard the vessel structures of the angiograms as outlier noise and represent vessels in the latent features.

Adversarial loss To generate both vessel segmentation masks and synthetic angiograms without the ground-truth labels, the proposed model is trained by adversarial learning using the two discriminators D_s and D_a . As shown in Figure 1, the discriminator D_s attempts to distinguish the estimated segmentation masks $\hat{\mathbf{s}}^v$ from the real fractal mask \mathbf{s}^f (in the (A) path), while the discriminator D_a tries to discriminate between the generated angiograms $\hat{\mathbf{x}}^a$ and the real angiography images \mathbf{x}_0^a (in the (B) path). As we employ LSGAN (Mao et al., 2017), the adversarial loss of generator \mathcal{L}_{adv}^G can be formulated by:

$$\mathcal{L}_{adv}^G(\epsilon_\theta, G, D_s, D_a) = \mathbb{E}_{\mathbf{x}^a} [(D_s(G(\epsilon_\theta(\mathbf{x}^a); \mathbf{0})) - 1)^2] + \mathbb{E}_{\mathbf{x}^a, \mathbf{s}^f} [(D_a(G(\epsilon_\theta(\mathbf{x}^b); \mathbf{s}^f)) - 1)^2]. \quad (13)$$

On the other hand, the discriminators are trained to compete against the generator with the adversarial loss functions, $\mathcal{L}_{adv}^{D_s}$ and $\mathcal{L}_{adv}^{D_a}$, which are defined by:

$$\mathcal{L}_{adv}^{D_s}(\epsilon_\theta, G, D_s) = \frac{1}{2} \mathbb{E}_{\mathbf{s}^f} [(D_s(\mathbf{s}^f) - 1)^2] + \frac{1}{2} \mathbb{E}_{\mathbf{x}^a} [(D_s(G(\epsilon_\theta(\mathbf{x}^a); \mathbf{0})))^2], \quad (14)$$

$$\mathcal{L}_{adv}^{D_a}(\epsilon_\theta, G, D_a) = \frac{1}{2} \mathbb{E}_{\mathbf{x}_0^a} [(D_a(\mathbf{x}_0^a) - 1)^2] + \frac{1}{2} \mathbb{E}_{\mathbf{x}^a, \mathbf{s}^f} [(D_a(G(\epsilon_\theta(\mathbf{x}^b); \mathbf{s}^f)))^2]. \quad (15)$$

This adversarial loss enables the single generator G to fool the discriminator D_s and D_a , by generating realistic segmentation masks $\hat{\mathbf{s}}^v = G(\epsilon_\theta(\mathbf{x}^a); \mathbf{0})$ and angiograms $\hat{\mathbf{x}}^a = G(\epsilon_\theta(\mathbf{x}^b); \mathbf{s}^f)$. In contrast, the discriminators attempt to distinguish these generated images being fake and the real images of \mathbf{s}^f and \mathbf{x}_0^a being real.

Cyclic reconstruction loss For the generator G to capture the semantic information of the vessels, we also constrain our model with the cyclic reconstruction loss on the fractal masks. Specifically, as the vessel-like fractal masks \mathbf{s}^f can be labels for the synthetic angiograms $\hat{\mathbf{x}}^a$ generated in the (B) path, we feed the $\hat{\mathbf{x}}^a$ into our model and reconstruct the fractal masks by the (A) path. Therefore, the cyclic reconstruction loss is computed between the reconstructed segmentation masks and the real fractal masks, which can be written by:

$$\mathcal{L}_{cyc}(\epsilon_\theta, G) = \mathbb{E}_{\mathbf{x}^b, \mathbf{s}^f} [|G(\epsilon_\theta(G(\epsilon_\theta(\mathbf{x}^b); \mathbf{s}^f); \mathbf{0}) - \mathbf{s}^f|_1]. \quad (16)$$

Here, we solve the segmentation problem as a vessel mask image generation, which is why we use L1 loss in the cyclic loss.

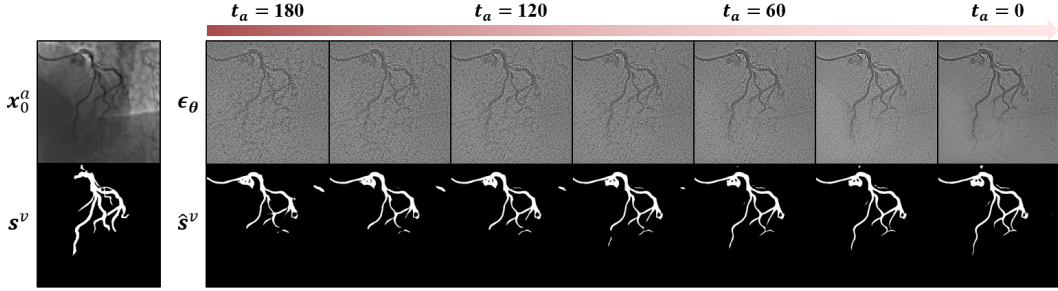


Figure 3: Vessel segmentation according to the noise level t_a . Our model estimates the segmentation masks \hat{s}^v using the latent features ϵ_θ for the noisy angiograms $x_{t_a}^a$. s^v is the ground-truth label.

3.1.2 IMAGE PERTURBATION FOR THE MODEL INPUT

Given real images of x_0^a and x_0^b , our diffusion module takes noisy angiograms $x_{t_a}^a$ in the (A) path and noisy background images $x_{t_b}^b$ in the (B) path as the input, in which each noisy image is sampled based on the forward diffusion process (2):

$$x_t = \sqrt{\alpha_t}x_0 + \sqrt{1 - \alpha_t}\epsilon, \quad (17)$$

where $\epsilon \sim \mathcal{N}(\mathbf{0}, \mathbf{I})$, and both of t_a and t_b are uniformly sampled time step in $[0, T]$. Here, for the diffusion module not only to learn the background image distribution in the (B) path but also to provide useful information for the generation module to segment the vessel structures under even certain noisy angiogram images in the (A) path, we sample t_a in the range of $[0, T_a]$ where $T_a < T$. Empirically, we found that this makes our model learn vessel representations robust to the noise.

3.2 INFERENCE OF VESSEL SEGMENTATION

The inference phase of DARN is different from the conventional diffusion model in that our model do not require iterative reverse process, similar to the recent diffusion-based unsupervised learning method called DiffuseMorph (Kim et al., 2021). Specifically, once the proposed DARN is trained, in the inference, we can obtain the vessel segmentation masks of angiograms from the (A) path by one step. For the noisy angiograms $x_{t_a}^a$ given by the forward diffusion process (17), our model provides the vessel segmentation masks using the latent features $\epsilon_\theta(x_{t_a}^a, t_a)$ estimated from the diffusion module. As shown in Figure 3, our model can generate the segmentation masks for any noise level t_a within a certain range (i.e. $[0, T_a]$). Nevertheless, since the angiography image x_0^a can be considered as one of the clean target images, the closer t_a is to zero, the better the vessel segmentation performance. Therefore, we test our model by setting $t_a = 0$.

4 EXPERIMENTS

In this section, we thoroughly evaluate the vessel segmentation performance of our method. We firstly compare the proposed DARN to existing unsupervised and self-supervised baseline models on various angiography datasets, including X-ray coronary angiography and retinal images. Also, we study the noise robustness of our model. Then, we analyze the success of our model in vessel representation and conduct an ablation study.

Datasets To realize the self-supervised learning framework, we train our model with the publicly available X-ray coronary angiography disease (XCAD) dataset obtained during stent placement surgery (Ma et al., 2021). A total of 1,621 angiography frames and their corresponding first frames, taken before injecting the contrast agents, are used as the real angiography and background images, respectively. Also, we generate 1,621 synthetic fractal masks by Ma et al. (2021). Additional 126 angiography images, along with the ground-truth vessel masks annotated by experienced radiologists, are divided into validation and test sets by 10% and 90%, respectively. We subsample all data into 256×256 . Also, in testing, we utilize two external X-ray coronary angiography (XCA) datasets acquired from different machines. 134 XCA dataset is composed of 134 angiography images with the vessel masks labeled by an expert cardiologist (Cervantes-Sanchez et al., 2019). 30 XCA dataset is composed of 30 sequences of angiography images (Hao et al., 2020). We utilize one angiography image from each sequence, along with its corresponding ground-truth vessel mask labeled by

experts. All the test images are resized to 512×512 . Furthermore, we evaluate cross-organ generalization capability on retinal imaging datasets. We use DRIVE (Staal et al., 2004) and STARE (Hoover & Goldbaum, 2003) datasets, each of which is composed of 20 retinal images and the corresponding expert-labeled vessel masks. Since retinal imaging is taken under high-resolution, we resize the image into 768×768 and split into 9 patches with 256×256 .

Implementation details Our model is implemented by employing the network architectures proposed in DDPM (Ho et al., 2020) and SPADE (Park et al., 2019) for the diffusion module and the generation module, respectively. Also, for the discriminators, we use the network of PatchGAN (Isola et al., 2017). To train the model, we set the number of time steps as $T = 2000$ with the linearly scheduled noise levels from 10^{-6} to 10^{-2} . Within this range, we sample the noisy angiograms by setting T_a to 200. Also, we set the hyperparameters of loss function as $\alpha = 0.2$ and $\beta = 5$. Our model is optimized by using the Adam algorithm (Kingma & Ba, 2014) with a learning rate of 5×10^{-6} on a single GPU card of Nvidia Quadro RTX 6000. We train the model for 150 epochs, and the model in the epoch with the best performance on the validation set is used for test data. All the implementations are done using the library of PyTorch (Paszke et al., 2019) in Python. The details of network structures and hyperparameter setting can be found in Appendix.

Baseline methods and metrics We compare our model to several baseline methods of un-/self-supervised learning, which do not require ground-truth vessel labels. For unsupervised learning methods, we utilize Spatial-Guided Clustering (SGC) (Ahn et al., 2021), Redrawing (Chen et al., 2019), and Deep Spectral (DS) (Melas-Kyriazi et al., 2022). For self-supervised learning methods, we employ Self-supervised Transformer with Energy-based Graph Optimization (STEGO) (Hamilton et al., 2022), Deep Adversarial (DA) (Mahmood et al., 2019), and Self-Supervised Vessel Segmentation (SSVS) (Ma et al., 2021). All these methods are implemented under identical training conditions to our model, unless the method needs no training procedure. For baseline methods that require heuristic thresholds, optimal performance is achieved by selecting data-specific thresholds

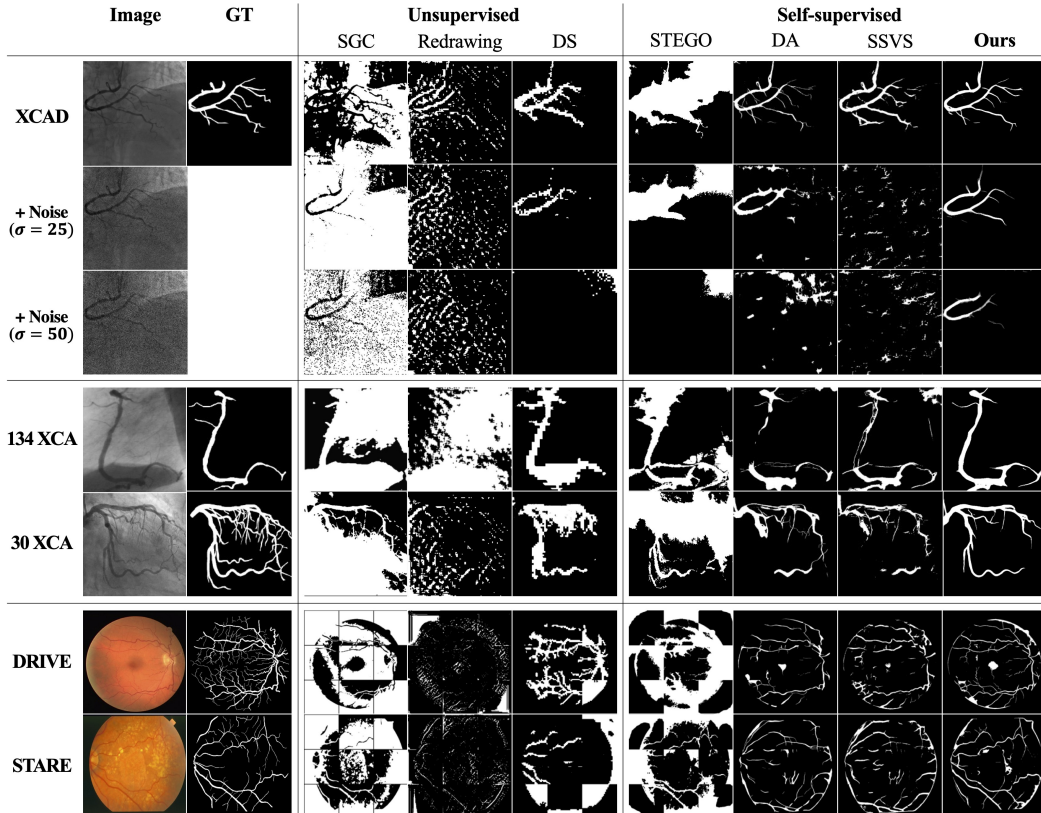


Figure 4: Visual comparison results on the vessel segmentation of various angiography images.

Table 1: Quantitative evaluation results on the vessel segmentation of various angiography images.

Data	Metric	Unsupervised			Self-supervised			
		SGC	Redrawing	DS	STEGO	DA	SSVS	Ours
Coronary angiography								
XCAD	IoU	0.060 \pm 0.034	0.059 \pm 0.032	0.366 \pm 0.105	0.146 \pm 0.070	0.375 \pm 0.066	0.410 \pm 0.087	0.471\pm0.076
	Dice	0.111 \pm 0.060	0.109 \pm 0.056	0.526 \pm 0.131	0.249 \pm 0.103	0.542 \pm 0.073	0.575 \pm 0.091	0.636\pm0.072
	Precision	0.062 \pm 0.034	0.139 \pm 0.081	0.469 \pm 0.127	0.152 \pm 0.077	0.557 \pm 0.115	0.590 \pm 0.119	0.701\pm0.115
134 XCA	IoU	0.045 \pm 0.035	0.056 \pm 0.018	0.256 \pm 0.110	0.134 \pm 0.081	0.190 \pm 0.155	0.318 \pm 0.128	0.426\pm0.059
	Dice	0.085 \pm 0.063	0.105 \pm 0.033	0.394 \pm 0.159	0.228 \pm 0.109	0.291 \pm 0.217	0.468 \pm 0.156	0.598\pm0.058
	Precision	0.047 \pm 0.036	0.058 \pm 0.019	0.280 \pm 0.123	0.136 \pm 0.088	0.506 \pm 0.201	0.592 \pm 0.125	0.781\pm0.118
30 XCA	IoU	0.083 \pm 0.039	0.048 \pm 0.022	0.339 \pm 0.086	0.191 \pm 0.072	0.298 \pm 0.109	0.324 \pm 0.146	0.427\pm0.184
	Dice	0.150 \pm 0.064	0.091 \pm 0.040	0.499 \pm 0.113	0.314 \pm 0.100	0.447 \pm 0.148	0.468 \pm 0.193	0.572\pm0.205
	Precision	0.090 \pm 0.041	0.144 \pm 0.074	0.525 \pm 0.130	0.200 \pm 0.081	0.612 \pm 0.174	0.613 \pm 0.212	0.729\pm0.152
Retinal imaging								
DRIVE	IoU	0.063 \pm 0.055	0.057 \pm 0.033	0.217 \pm 0.143	0.152 \pm 0.073	0.245 \pm 0.090	0.314 \pm 0.101	0.372\pm0.148
	Dice	0.115 \pm 0.093	0.105 \pm 0.059	0.333 \pm 0.201	0.257 \pm 0.106	0.386 \pm 0.117	0.469 \pm 0.119	0.528\pm0.161
	Precision	0.069 \pm 0.061	0.199 \pm 0.155	0.243 \pm 0.175	0.169 \pm 0.100	0.503 \pm 0.218	0.549 \pm 0.216	0.617\pm0.271
STARE	IoU	0.055 \pm 0.045	0.074 \pm 0.048	0.180 \pm 0.141	0.125 \pm 0.076	0.237 \pm 0.122	0.311 \pm 0.148	0.368\pm0.191
	Dice	0.101 \pm 0.077	0.134 \pm 0.080	0.281 \pm 0.201	0.216 \pm 0.109	0.367 \pm 0.167	0.454 \pm 0.185	0.508\pm0.216
	Precision	0.058 \pm 0.047	0.227 \pm 0.157	0.205 \pm 0.172	0.135 \pm 0.092	0.427 \pm 0.233	0.490 \pm 0.230	0.537\pm0.280

within the range from 0.2 to 0.8 in increments of 0.1. To quantitatively evaluate the segmentation performance, we compute Intersection over Union (IoU), Dice similarity coefficient, and Precision.

4.1 EXPERIMENTAL RESULTS

Figure 4 shows the vessel segmentation masks from the baseline methods and our proposed method on three different coronary angiography datasets and two retinal imaging datasets. Quantitative evaluation results of the methods are presented in Table 1. The analysis of the results is as follows.

Comparison of ours to baselines When we compare the proposed method to the baselines, our model segments vessel structures including tiny branches more accurately. Also, as shown in Table 1, our model consistently achieves the SOTA performance by large margin compared to existing unsupervised and self-supervised methods. In specific, our network shows significantly improved precision scores, which demonstrates advantages of our DARN that effectively differentiates foreground vessel structure and eliminates false positive signals from the noisy backgrounds.

Generalization capability To verify that our trained DARN can be generally applied to various vessel image taken from different machines or different anatomic region-of-interests (ROI), we also study the generalization capability of our method. First, when we test our model on external 134 XCA and 30 XCA datasets directly, which have different resolutions and noise distributions to those of the XCAD dataset, as shown in Figure 4 and Table 1, our model achieves higher performance than the others. Moreover, when we evaluate the model on DRIVE and STARE retinal datasets that have unseen data distribution of different modalities and ROIs from the XCAD, our DARN shows the most promising cross-organ generalization performance. This may come from the proposed adversarial framework that reuses the generated angiography images for the segmentation process through the cycle path, diversifying the input data distribution. Also, the diffusion module learning the stochastic diffusion process enables our model to be used in general for vessel segmentation.

Robustness to noises As X-ray images are often acquired under low-dose radiation exposure to reduce potential risks, we further evaluate the performance of our model on simulated noisy angiograms. Using the XCAD dataset, we add Gaussian noise to the angiogram with different levels of $\sigma = 10, 25$, and 50 . We show the segmentation results according to the noise levels in Figure 4. Also, we report the quantitative evaluation results in Table 2. It is noteworthy that our DARN is the only method to segment vessel structures with reasonable performance under noise corruption. Since the proposed segmentation method is trained through the diffusion module that perturbs the input images, the model is highly robust to segment vessel structure even from the noisy data.

Latent representation To study the origin of the performance improvement, in Figure 5, we show the latent features $\epsilon_\theta(x_t, t)$ given x_0 for (A) the angiography $x_0 = x_0^a$ and (B) the

Table 2: Results of noise robustness test according to the Gaussian noise with σ .

σ	Metric	Unsupervised			Self-supervised			
		SGC	Redrawing	DS	STEGO	DA	SSVS	Ours
10	IoU	0.066 \pm 0.033	0.052 \pm 0.031	0.331 \pm 0.104	0.144 \pm 0.073	0.353 \pm 0.065	0.258 \pm 0.079	0.451\pm0.080
	Dice	0.122 \pm 0.059	0.096 \pm 0.053	0.487 \pm 0.133	0.245 \pm 0.107	0.519 \pm 0.073	0.404 \pm 0.099	0.617\pm0.076
	Precision	0.069 \pm 0.035	0.126 \pm 0.077	0.480 \pm 0.135	0.157 \pm 0.091	0.481 \pm 0.104	0.477 \pm 0.117	0.710\pm0.115
25	IoU	0.069 \pm 0.035	0.036 \pm 0.021	0.232 \pm 0.094	0.118 \pm 0.064	0.247 \pm 0.072	0.059 \pm 0.033	0.389\pm0.088
	Dice	0.128 \pm 0.061	0.069 \pm 0.039	0.366 \pm 0.132	0.206 \pm 0.095	0.391 \pm 0.092	0.109 \pm 0.058	0.554\pm0.092
	Precision	0.072 \pm 0.036	0.095 \pm 0.058	0.446 \pm 0.159	0.144 \pm 0.115	0.371 \pm 0.106	0.149 \pm 0.082	0.727\pm0.119
50	IoU	0.070 \pm 0.025	0.020 \pm 0.012	0.077 \pm 0.065	0.060 \pm 0.050	0.102 \pm 0.056	0.021 \pm 0.013	0.269\pm0.081
	Dice	0.130 \pm 0.045	0.040 \pm 0.022	0.136 \pm 0.109	0.108 \pm 0.088	0.180 \pm 0.091	0.041 \pm 0.025	0.417\pm0.101
	Precision	0.072 \pm 0.026	0.061 \pm 0.038	0.221 \pm 0.168	0.076 \pm 0.067	0.169 \pm 0.094	0.060 \pm 0.038	0.716\pm0.147

backgrounds $\mathbf{x}_0 = \mathbf{x}_0^b$ with $t = 100$, respectively. In contrast to the (B) path, the latent representation in the (A) path emphasizes the vessel structures. This implies that although there are no ground-truth labels, our model learns the background image representation so that the vessel structure can be captured as outlier noise, leading to improved segmentation performance.

Ablation study Table 3 shows the quantitative evaluation results of several ablation studies, and visual results are in Appendix. (a) Our model without the diffusion module and \mathcal{L}_{diff} shows lower performance by about 5% for all metrics compared to our model, which suggests that the diffusion module guides the generation module to extract vessel representation accurately. (b) The generation module without the proposed SPADE layers is degraded by more than 5% over (a) for all metrics, verifying that our SPADE-based unified generator effectively captures vessel semantic information through the synergy of learning both image segmentation and generation. (c) Through the implementation of our model without the proposed cyclic loss \mathcal{L}_{cyc} , we verify that \mathcal{L}_{cyc} allows our model to segment proper vessel regions. (d) When training our model by converting the L1 loss for \mathcal{L}_{cyc} to the cross-entropy (CE) loss, the performance is much worse than ours in all metrics, which implies that our approach using L1 loss for the cycle path is proper to obtain the vessel masks.

Table 3: Results of ablation study on the proposed model and loss function.

Method	Module		Loss function			Metric		
	Diffusion	Generation	\mathcal{L}_{diff}	\mathcal{L}_{adv}	\mathcal{L}_{cyc}	IoU	Dice	Precision
Ours	✓	✓	✓	✓	✓	0.471\pm0.076	0.636\pm0.072	0.701\pm0.115
(a)		✓		✓	✓	0.420 \pm 0.081	0.587 \pm 0.084	0.606 \pm 0.101
(b)		w/o S-SPADE		✓	✓	0.362 \pm 0.065	0.528 \pm 0.072	0.483 \pm 0.102
(c)	✓	✓	✓	✓	✓	0.322 \pm 0.055	0.485 \pm 0.064	0.580 \pm 0.112
(d)	✓	✓	✓	✓	L1 \rightarrow CE	0.346 \pm 0.084	0.508 \pm 0.094	0.672 \pm 0.147

5 CONCLUSION

We present a non-iterative diffusion model called DARN for self-supervised vessel segmentation. Our model composed of the diffusion and generation modules learns vessel representation without labels via adversarial learning, in the guidance of latent features estimated from the diffusion module. Also, through the proposed switchable SPADE layer, we generate synthetic angiograms as well as vessel segmentation masks, leading to learning semantic information about vessels more effectively. Although the diffusion module training is combined with other loss functions, the inference is not iterative but only done in one step, which makes it faster and unique compared to the existing diffusion models. Using various medical vessel datasets, we verify that our model is much superior to existing un-/self-supervised learning methods. Moreover, thanks to the diffusion module, our model is robust to image diversity and noise, suggesting that our model can be an important platform for designing a general vessel segmentation model.

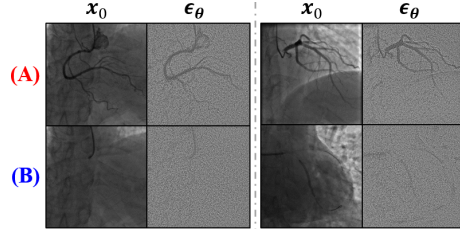


Figure 5: Estimated latent features ϵ_θ in the (A) and (B) paths of our model.

REFERENCES

Euijoon Ahn, Dagan Feng, and Jinman Kim. A spatial guided self-supervised clustering network for medical image segmentation. In *International Conference on Medical Image Computing and Computer-Assisted Intervention*, pp. 379–388. Springer, 2021.

Tomer Amit, Eliya Nachmani, Tal Shaharbany, and Lior Wolf. Segdiff: Image segmentation with diffusion probabilistic models. *arXiv preprint arXiv:2112.00390*, 2021.

Dmitry Baranchuk, Andrey Voynov, Ivan Rubachev, Valentin Khrulkov, and Artem Babenko. Label-efficient semantic segmentation with diffusion models. In *International Conference on Learning Representations*, 2021.

Fernando Cervantes-Sanchez, Ivan Cruz-Aceves, Arturo Hernandez-Aguirre, Martha Alicia Hernandez-Gonzalez, and Sergio Eduardo Solorio-Meza. Automatic segmentation of coronary arteries in x-ray angiograms using multiscale analysis and artificial neural networks. *Applied Sciences*, 9(24), 2019. ISSN 2076-3417. doi: 10.3390/app9245507. URL <https://www.mdpi.com/2076-3417/9/24/5507>.

Mickaël Chen, Thierry Artières, and Ludovic Denoyer. Unsupervised object segmentation by redrawing. *Advances in neural information processing systems*, 32, 2019.

Yang Chen, Luyao Shi, Qianjing Feng, Jian Yang, Huazhong Shu, Limin Luo, Jean-Louis Coatrieux, and Wufan Chen. Artifact suppressed dictionary learning for low-dose ct image processing. *IEEE transactions on medical imaging*, 33(12):2271–2292, 2014.

Hyungjin Chung, Byeongsu Sim, and Jong Chul Ye. Come-closer-diffuse-faster: Accelerating conditional diffusion models for inverse problems through stochastic contraction. In *Proceedings of the IEEE/CVF Conference on Computer Vision and Pattern Recognition*, pp. 12413–12422, 2022.

Weijian Cong, Jian Yang, Danni Ai, Yang Chen, Yue Liu, and Yongtian Wang. Quantitative analysis of deformable model-based 3-d reconstruction of coronary artery from multiple angiograms. *IEEE Transactions on Biomedical Engineering*, 62(8):2079–2090, 2015.

Jingfan Fan, Jian Yang, Yachen Wang, Siyuan Yang, Danni Ai, Yong Huang, Hong Song, Aimin Hao, and Yongtian Wang. Multichannel fully convolutional network for coronary artery segmentation in x-ray angiograms. *Ieee Access*, 6:44635–44643, 2018.

Mark Hamilton, Zhoutong Zhang, Bharath Hariharan, Noah Snavely, and William T Freeman. Unsupervised semantic segmentation by distilling feature correspondences. *arXiv preprint arXiv:2203.08414*, 2022.

Dongdong Hao, Song Ding, Linwei Qiu, Yisong Lv, Baowei Fei, Yueqi Zhu, and Binjie Qin. Sequential vessel segmentation via deep channel attention network. *Neural Networks*, 128:172–187, 2020. ISSN 0893-6080. doi: <https://doi.org/10.1016/j.neunet.2020.05.005>. URL <https://www.sciencedirect.com/science/article/pii/S0893608020301672>.

Kaiming He, Xiangyu Zhang, Shaoqing Ren, and Jian Sun. Deep residual learning for image recognition. In *Proceedings of the IEEE conference on computer vision and pattern recognition*, pp. 770–778, 2016.

Jonathan Ho, Ajay Jain, and Pieter Abbeel. Denoising diffusion probabilistic models. *Advances in Neural Information Processing Systems*, 33:6840–6851, 2020.

Adam Hoover and Michael Goldbaum. Locating the optic nerve in a retinal image using the fuzzy convergence of the blood vessels. *IEEE transactions on medical imaging*, 22(8):951–958, 2003.

Phillip Isola, Jun-Yan Zhu, Tinghui Zhou, and Alexei A Efros. Image-to-image translation with conditional adversarial networks. In *Proceedings of the IEEE conference on computer vision and pattern recognition*, pp. 1125–1134, 2017.

Boah Kim, Inhwa Han, and Jong Chul Ye. Diffusemorph: Unsupervised deformable image registration along continuous trajectory using diffusion models. *arXiv preprint arXiv:2112.05149*, 2021.

Diederik P Kingma and Jimmy Ba. Adam: A method for stochastic optimization. *arXiv preprint arXiv:1412.6980*, 2014.

Max WK Law and Albert CS Chung. Efficient implementation for spherical flux computation and its application to vascular segmentation. *IEEE transactions on image processing*, 18(3):596–612, 2009.

Andreas Lugmayr, Martin Danelljan, Andres Romero, Fisher Yu, Radu Timofte, and Luc Van Gool. Repaint: Inpainting using denoising diffusion probabilistic models. In *Proceedings of the IEEE/CVF Conference on Computer Vision and Pattern Recognition*, pp. 11461–11471, 2022.

Yuxin Ma, Yang Hua, Hanming Deng, Tao Song, Hao Wang, Zhengui Xue, Heng Cao, Ruhui Ma, and Haibing Guan. Self-supervised vessel segmentation via adversarial learning. In *Proceedings of the IEEE/CVF International Conference on Computer Vision*, pp. 7536–7545, 2021.

Faisal Mahmood, Daniel Borders, Richard J Chen, Gregory N McKay, Kevan J Salimian, Alexander Baras, and Nicholas J Durr. Deep adversarial training for multi-organ nuclei segmentation in histopathology images. *IEEE transactions on medical imaging*, 39(11):3257–3267, 2019.

Xudong Mao, Qing Li, Haoran Xie, Raymond YK Lau, Zhen Wang, and Stephen Paul Smolley. Least squares generative adversarial networks. In *Proceedings of the IEEE international conference on computer vision*, pp. 2794–2802, 2017.

Luke Melas-Kyriazi, Christian Rupprecht, Iro Laina, and Andrea Vedaldi. Deep spectral methods: A surprisingly strong baseline for unsupervised semantic segmentation and localization. In *Proceedings of the IEEE/CVF Conference on Computer Vision and Pattern Recognition*, pp. 8364–8375, 2022.

Ebrahim Nasr-Esfahani, Shadrokh Samavi, Nader Karimi, SM Reza Soroushmehr, Kevin Ward, Mohammad H Jafari, Banafsheh Felfeliyan, B Nallamothu, and Kayvan Najarian. Vessel extraction in x-ray angiograms using deep learning. In *2016 38th Annual international conference of the IEEE engineering in medicine and biology society (EMBC)*, pp. 643–646. IEEE, 2016.

Yujin Oh and Jong Chul Ye. CXR Segmentation by AdaIN-based Domain Adaptation and Knowledge Distillation. *arXiv preprint arXiv:2104.05892*, 2021.

Taesung Park, Ming-Yu Liu, Ting-Chun Wang, and Jun-Yan Zhu. Semantic image synthesis with spatially-adaptive normalization. In *Proceedings of the IEEE/CVF conference on computer vision and pattern recognition*, pp. 2337–2346, 2019.

Adam Paszke, Sam Gross, Francisco Massa, Adam Lerer, James Bradbury, Gregory Chanan, Trevor Killeen, Zeming Lin, Natalia Gimelshein, Luca Antiga, et al. Pytorch: An imperative style, high-performance deep learning library. *Advances in neural information processing systems*, 32, 2019.

Olaf Ronneberger, Philipp Fischer, and Thomas Brox. U-net: Convolutional networks for biomedical image segmentation. In *International Conference on Medical image computing and computer-assisted intervention*, pp. 234–241. Springer, 2015.

Chitwan Saharia, Jonathan Ho, William Chan, Tim Salimans, David J Fleet, and Mohammad Norouzi. Image super-resolution via iterative refinement. *arXiv preprint arXiv:2104.07636*, 2021.

Chitwan Saharia, William Chan, Huiwen Chang, Chris Lee, Jonathan Ho, Tim Salimans, David Fleet, and Mohammad Norouzi. Palette: Image-to-image diffusion models. In *ACM SIGGRAPH 2022 Conference Proceedings*, pp. 1–10, 2022.

Jascha Sohl-Dickstein, Eric Weiss, Niru Maheswaranathan, and Surya Ganguli. Deep unsupervised learning using nonequilibrium thermodynamics. In *International Conference on Machine Learning*, pp. 2256–2265. PMLR, 2015.

Yang Song and Stefano Ermon. Generative modeling by estimating gradients of the data distribution. *Advances in Neural Information Processing Systems*, 32, 2019.

Yang Song, Jascha Sohl-Dickstein, Diederik P Kingma, Abhishek Kumar, Stefano Ermon, and Ben Poole. Score-based generative modeling through stochastic differential equations. In *International Conference on Learning Representations*, 2020.

Joes Staal, Michael D Abràmoff, Meindert Niemeijer, Max A Viergever, and Bram Van Ginneken. Ridge-based vessel segmentation in color images of the retina. *IEEE transactions on medical imaging*, 23(4):501–509, 2004.

Maryam Taghizadeh Dehkordi, Ali Mohamad Doost Hoseini, Saeed Sadri, and Hamid Soltanianzadeh. Local feature fitting active contour for segmenting vessels in angiograms. *IET Computer Vision*, 8(3):161–170, 2014.

Dmitry Ulyanov, Andrea Vedaldi, and Victor Lempitsky. Improved texture networks: Maximizing quality and diversity in feed-forward stylization and texture synthesis. In *Proceedings of the IEEE conference on computer vision and pattern recognition*, pp. 6924–6932, 2017.

Shaoyan Xia, Haogang Zhu, Xiaoli Liu, Ming Gong, Xiaoyong Huang, Lei Xu, Hongjia Zhang, and Jialong Guo. Vessel segmentation of x-ray coronary angiographic image sequence. *IEEE Transactions on Biomedical Engineering*, 67(5):1338–1348, 2019.

Jun-Yan Zhu, Taesung Park, Phillip Isola, and Alexei A Efros. Unpaired image-to-image translation using cycle-consistent adversarial networks. In *Proceedings of the IEEE international conference on computer vision*, pp. 2223–2232, 2017.

A DETAILS OF NETWORK ARCHITECTURE

In this section, we provide details of the generator G proposed in our diffusion adversarial representation learning (DARL) model, which is composed of the diffusion module and the generation module. For the diffusion module, we adapt the network architecture of DDPM (Ho et al., 2020) that has U-Net (Ronneberger et al., 2015) structure, as described in Table 4. The generation module is composed of four consecutive residual blocks (He et al., 2016) with switchable spatially-adaptive denormalization (SPADE) layers, as described in Table 5.

Table 4: Detailed network architecture of the diffusion module. For each block (blk), $C_{i,j}$ is the convolution layer with $i \times i$ kernel and stride length of j , RS_i pairs are entry points for residual shortcut path within a block unit, RB is the residual block module, and SA is the self-attention module. GN is the group normalization, and Ch indicates the size of output channel dimension.

Blk	Diffusion module												Ch	
	Downstream						Upstream							
1	$C_{3,1}$	RS_1	RB	RS_2	RB	RS_3	RS_3	RB	RS_2	RB	RS_1	RB	CB	1
2	$C_{3,2}$	RS_1	RB	RS_2	RB	RS_3	RS_3	RB	RS_2	RB	RS_1	RB	UP	64
3	$C_{3,2}$	RS_1	RB	RS_2	RB	RS_3	RS_3	RB	RS_2	RB	RS_1	RB	UP	128
4	$C_{3,2}$	RS_1	RB	RS_2	RB	RS_3	RS_3	RB	RS_2	RB	RS_1	RB	UP	128
5	$C_{3,2}$	RS_1	RB SA	RS_2	RB SA	RS_3	RS_3	RB SA	RS_2	RB SA	RS_1	RB SA	UP	256
6	$C_{3,2}$	RS_1	RB	RS_2	RB	RS_3	RS_3	RB	RS_2	RB	RS_1	RB	UP	256
Mid						SA		RB						

Note: RB = $[RS_n - \text{GN} - \text{Swish} - C_{3,1} - \text{GN} - \text{Swish} - C_{3,1} - RS_n]$, SA = $[\text{GN} - C_1 - C_1]$,
 UP = [Upsample - $C_{3,1}$], CB = $[\text{GN} - \text{Swich} - C_3]$

Table 5: Detailed network architecture of the generation module. UP is the nearest neighbor upsampling function, RS_i pairs are entry points for residual shortcut path, $C_{i,j}$ is the convolution layer with $i \times i$ kernel and stride length of j , and IN is the instance normalization layer. S-SPADE is the proposed switchable SPADE layer that turns on SPADE if the semantic layout is provided, otherwise turns off SPADE and applies IN. Ch indicates the size of output channel dimension.

Stream	Generation module							Ch
	Scale	Conv.	Act.	Norm.	Conv.	Act.	Norm.	
In		C_7		IN		ReLU		64
DownBlock1		$C_{3,2}$		IN		ReLU		128
DownBlock2		$C_{3,2}$		IN		ReLU		256
MidResBlock1	RS_1	$C_{3,1}$	ReLU	S-SPADE	$C_{3,1}$	ReLU	S-SPADE	RS_1
MidResBlock2	RS_2	$C_{3,1}$	ReLU	S-SPADE	$C_{3,1}$	ReLU	S-SPADE	RS_2
UpResBlock1	UP	RS_3	$C_{3,1}$	ReLU	S-SPADE	$C_{3,1}$	ReLU	S-SPADE
UpResBlock2	UP	RS_4	$C_{3,1}$	ReLU	S-SPADE	$C_{3,1}$	ReLU	S-SPADE
Out		C_7						1

B ADDITIONAL EXPERIMENTAL RESULTS

Study on synthetic angiogram generation As described in the main paper, a single generation module with the switchable SPADE layers in our model provides both the synthetic angiograms and the vessel segmentation masks by one-step inference, compared to iterative inference steps of other diffusion models. To evaluate the angiogram synthesis performance, we compare our model with the methods of DA and SSVS. These baselines generate the segmentation masks and the synthetic angiograms, but unlike ours, they use two different networks employing the CycleGAN (Zhu et al., 2017) framework. Figure 6 compares the visual results of synthetic angiograms using the backgrounds and fractal masks. Compared to the others, our generation module yields the most realistic images that naturally reflect fractal masks on the background and also contain even tiny branches. This allows our model to maintain the cycle consistency on the vessel-like fractal signals and capture vessel semantic information effectively, leading to the improvement of segmentation performance.

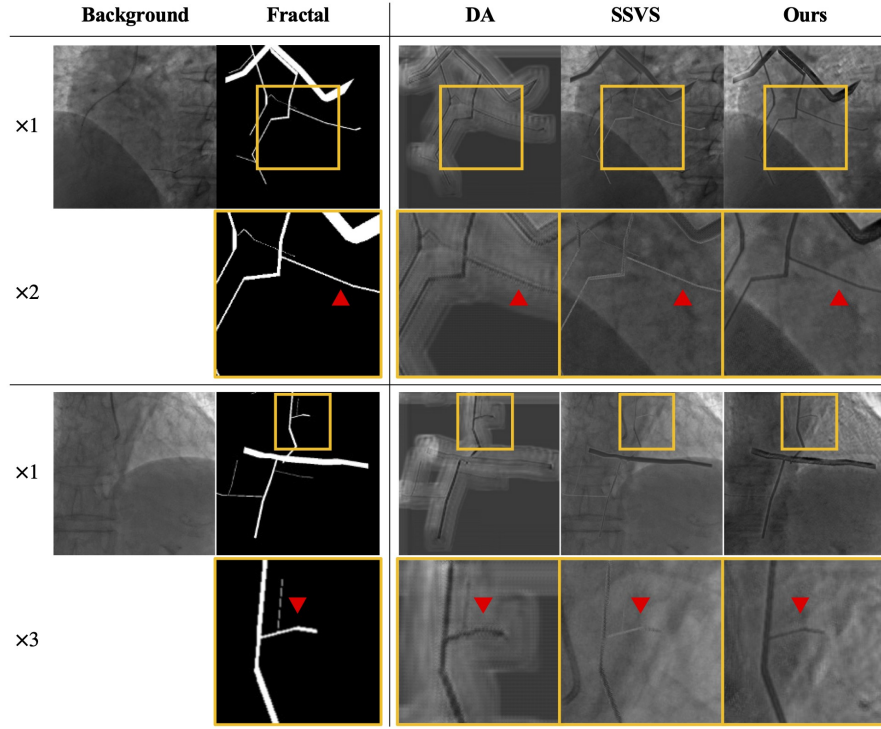


Figure 6: Visual comparison results of the generated fake angiograms. Yellow boxes in $\times 1$ rows are magnified by two or three times in the corresponding bottom rows, respectively. Red triangles indicate remarkable points.

Study on hyperparameter setting In the main paper, we report the vessel segmentation results from the model trained with $\alpha = 0.2$ and $\beta = 5$ based on the study of hyperparameter setting, which yields optimal performance in our experiments. To study the effects of hyperparameters on the segmentation performance, using the proposed loss function, we trained our model with the fixed $\beta = 5.0$ when adjusting the parameter α . Similarly, α is fixed with 0.2 when β is adjusted. Figure 7 shows graphs of the quantitative evaluation results of IoU, Dice, and Precision metrics according to the hyperparameters of α and β . We can see that our model can learn the semantic vessel segmentation when the parameter α that controls the adversarial loss \mathcal{L}_{adv} is equal to or more than 0.2, though the performance gradually decreases as α increases. Also, the results show that the highest performance for all metrics is achieved when $\alpha = 0.2$. On the other hand, while our model hardly captures the semantic information of vessels when there is no cycle path in network training (i.e. $\beta = 0$), the model can provide plausible vessel segmentation masks as long as the cycle path exists. Also, when we investigate the segmentation performance according to the β that weights the cyclic loss \mathcal{L}_{cyc} , the optimal performance is obtained when $\beta = 5.0$.

Study on the angiogram perturbation in model training When training our model, the background images are perturbed by the forward diffusion process with the uniformly sampled time step $t_b \in [0, T]$, whereas the angiograms are perturbed with the time step $t_a \in [0, T_a]$ where $T_a < T$. To investigate the effect of time step size T_a for the angiogram perturbation on model performance, we train our model with different time step sizes by setting T_a as 100, 200, 500, and 1000. Figure 8 shows the quantitative evaluation results. When T_a is less than 200, the vessel segmentation performance on the clean angiograms gets better, but the performance is degraded on the simulated low-dose angiograms corrupted by Gaussian noise with σ levels of 25 and 50. Also, when T_a is set over 500, the model shows drastically low performance due to the lack of vascular information from the noisy angiograms. These results imply that the diffusion module can optimally provide latent features including vascular structures as long as the model is trained in the setting of $T_a \leq 200$. Also, the proposed implementation makes our DARN robust to noise, which suggests that our model can segment vascular structures even on low-dose medical images.

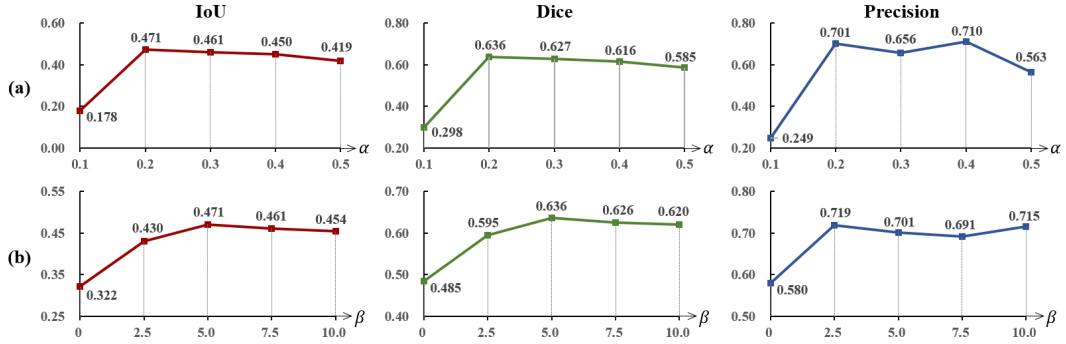


Figure 7: Vessel segmentation performance of our model on the XCAD dataset according to the hyper-parameters of the proposed loss function. Each column shows the average values of quantitative evaluation results with respect to (a) α for the adversarial loss \mathcal{L}_{adv} and (b) β for the cyclic reconstruction loss \mathcal{L}_{cyc} .

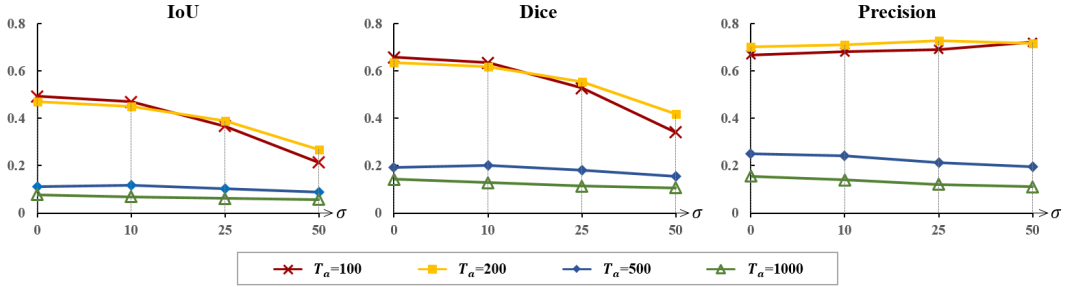


Figure 8: Vessel segmentation performance of our model according to the settings of T_a for the angiogram perturbation. Each graph shows the quantitative evaluation results with respect to the Gaussian noise level σ .

Study on the adversarial learning with two discriminators Our proposed model is trained via adversarial learning with two discriminators D_s and D_a that distinguish real and fake segmentation masks and angiograms, respectively. To confirm that this discriminator setting is optimal, we additionally conduct experiments to train our model without either D_s or D_a . As reported in Table 6(a), the model trained without D_s slightly increases the precision but degrades the scores for the IoU and Dice metrics. Also, the model trained without D_a shows inferior segmentation performance as shown in Table 6(b), which may be due to the failure to generate realistic angiograms, making the model relatively hard to learn vessel semantic information. These results suggest that our model with both D_s and D_a is optimal to learn vessel representations.

Table 6: Vessel segmentation performance of our model without the discriminator D_s/D_a .

Method	Discriminators		Metric		
	D_s	D_a	IoU	Dice	Precision
Ours	✓	✓	0.471\pm0.076	0.636\pm0.072	0.701 \pm 0.115
(a)		✓	0.456 \pm 0.081	0.622 \pm 0.078	0.728\pm0.117
(b)	✓		0.348 \pm 0.061	0.513 \pm 0.069	0.496 \pm 0.106

Qualitative comparison results of the ablation study For the ablation studies in the main paper, we show the visual comparison results in Figure 9. The results of (a) and (b) show that our model trained without the diffusion module generates the vessel masks including many false positive regions. When compared ours with (c), we can observe that the cycle consistency on the fake vessels allows our model to segment tiny vessels more accurately. Moreover, the comparison of (d) and ours verify that the proposed model achieves better performance, although we solve the segmentation problem with the image generation in that we use L1 loss for the segmentation masks.

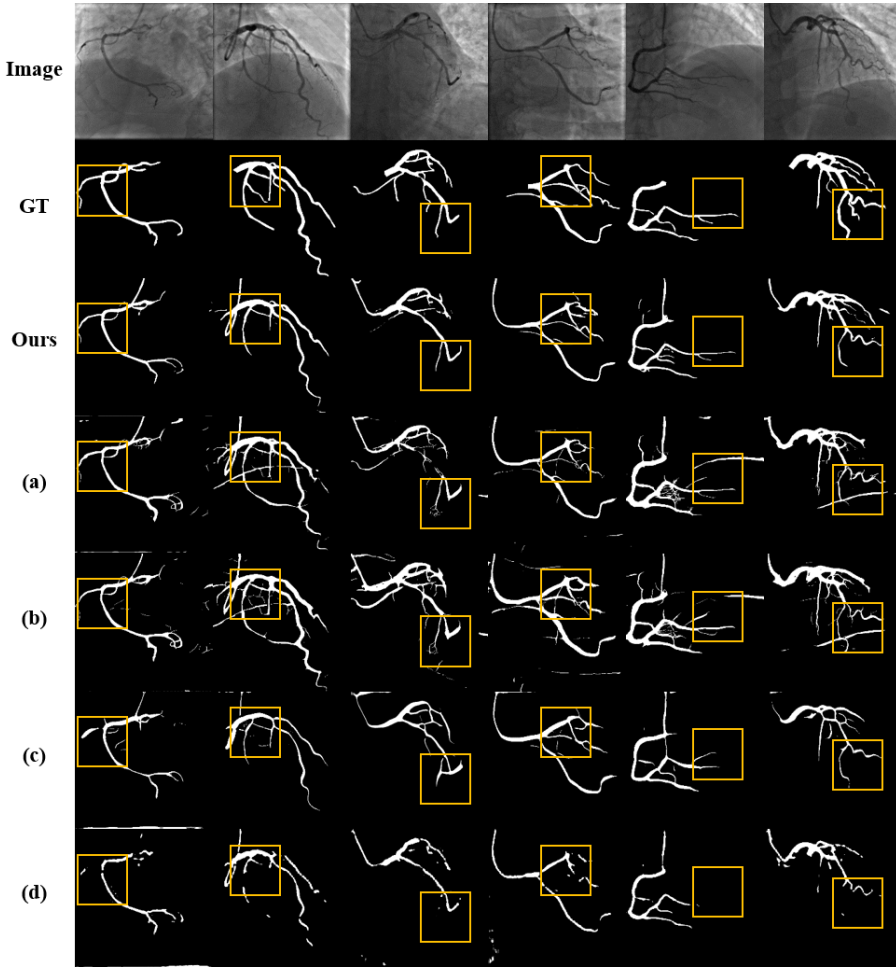


Figure 9: Visual comparison results of the ablation study. (a-d) correspond to each case study (a-d) in Table 3 of the main paper. Yellow boxes denote remarkable parts.

C ADDITIONAL VISUAL COMPARISON RESULTS

In this section, we provide additional vessel segmentation results that show the success of our DARN in self-supervised segmentation. Figure 10 shows that our model consistently provides the best performance on XCAD dataset. Also, our model segments vascular structures better than the other baselines even on the external angiography datasets (134 XCA and 30 XCA) and the retinal image datasets (DRIVE and STARE). These results suggest that the proposed model can be used as a general vessel segmentation model for various vascular images. Also, Figure 11 shows the vessel segmentation results on the XCAD data that are corrupted by Gaussian noise with different levels of σ . The visual results demonstrate that our DARN is the only method which endures harsh corruption and outperforms the baseline methods.

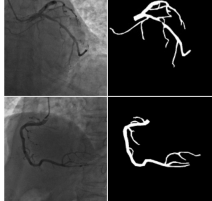
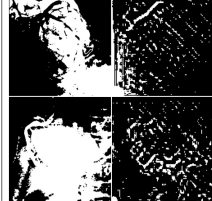
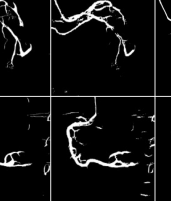
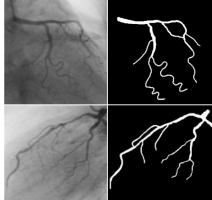
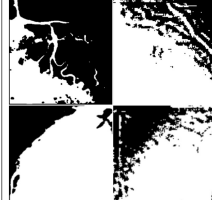
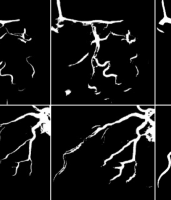
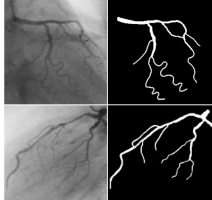
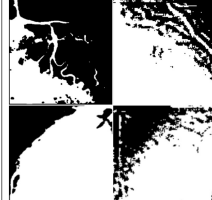
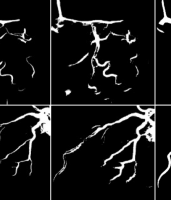
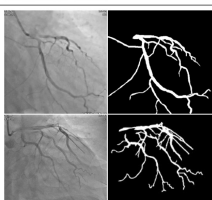
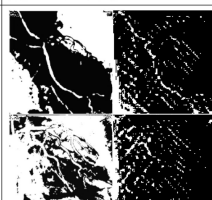
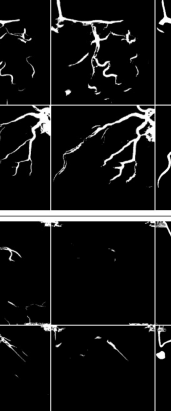
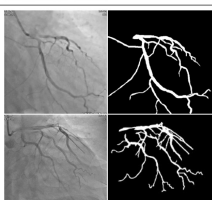
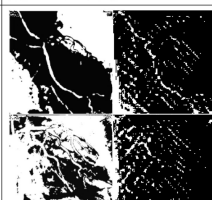
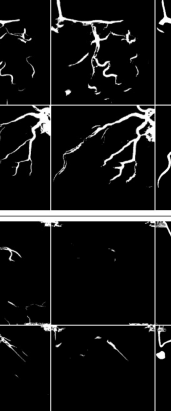
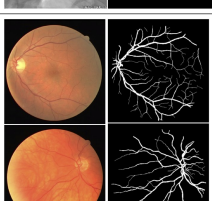
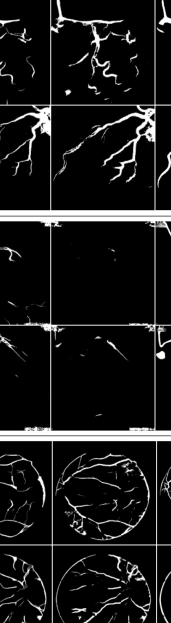
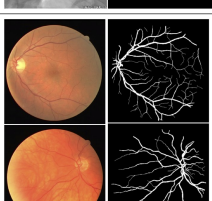
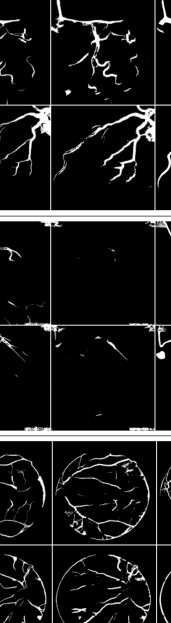
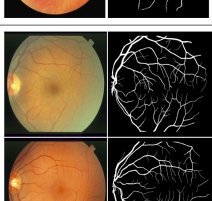
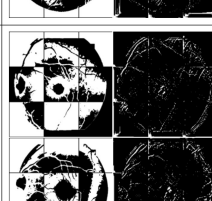
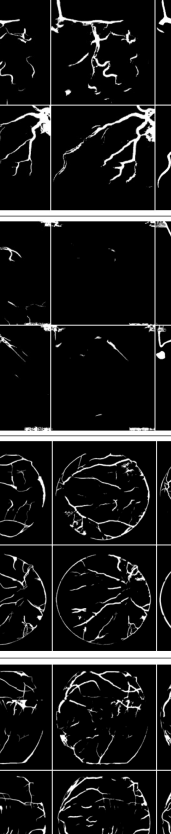
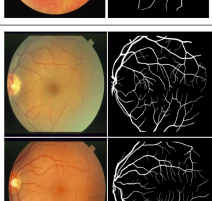
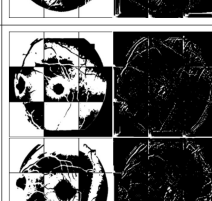
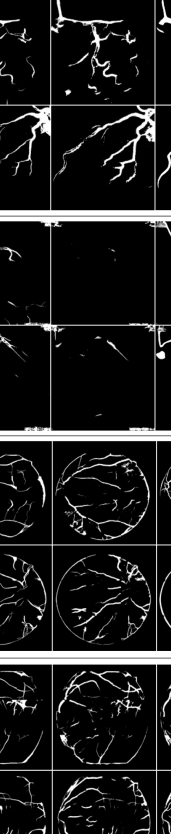
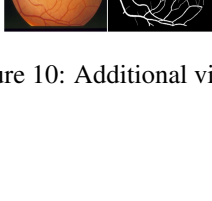
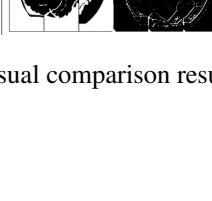
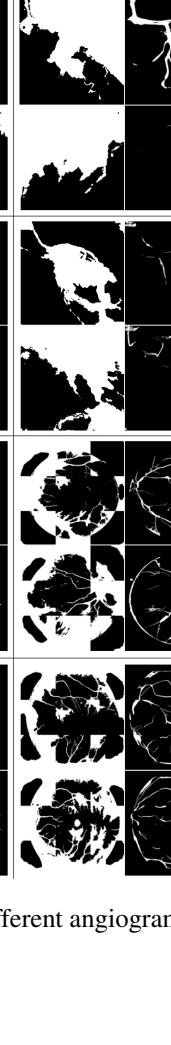
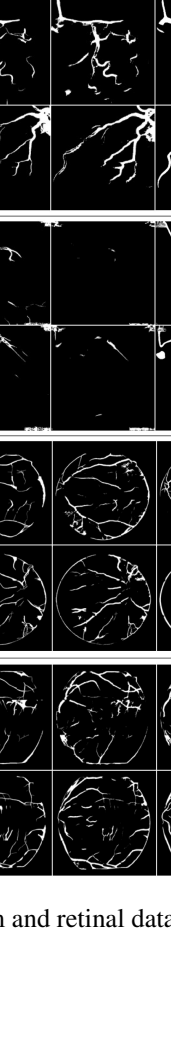
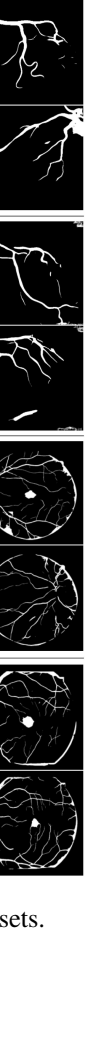
Image	GT	Unsupervised			Self-supervised			Ours	
		SGC	Redrawing	DS	STEGO	DA	SSVS		
XCAD									
									
134 XCA									
									
30 XCA									
									
DRIVE									
									
STARE									
									

Figure 10: Additional visual comparison results on different angiogram and retinal datasets.

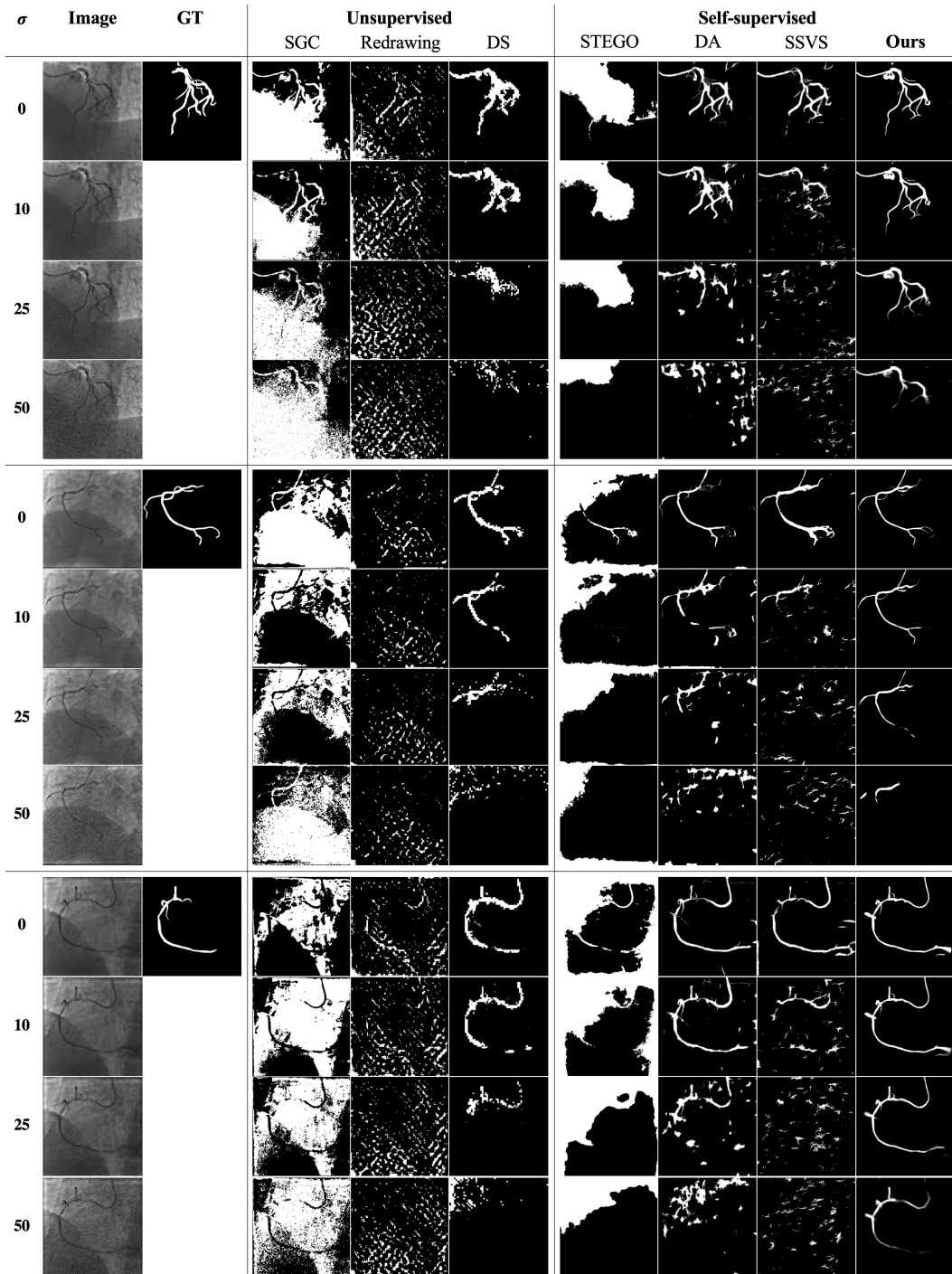


Figure 11: Additional visual comparison results on XCAD datasets with different levels (σ) of Gaussian noise.